Supplementary Information

Supplementary Figure 1

a

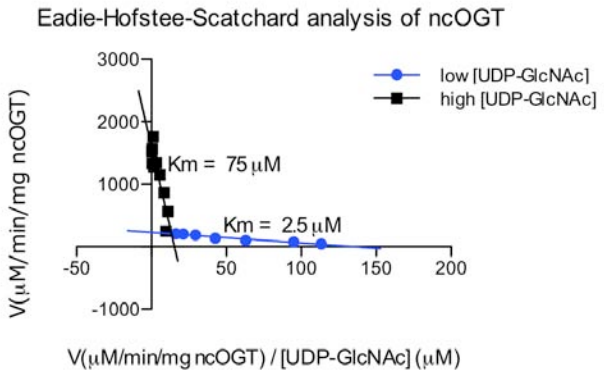

b

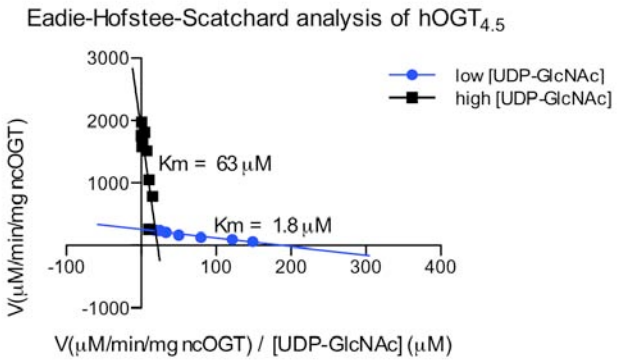

c

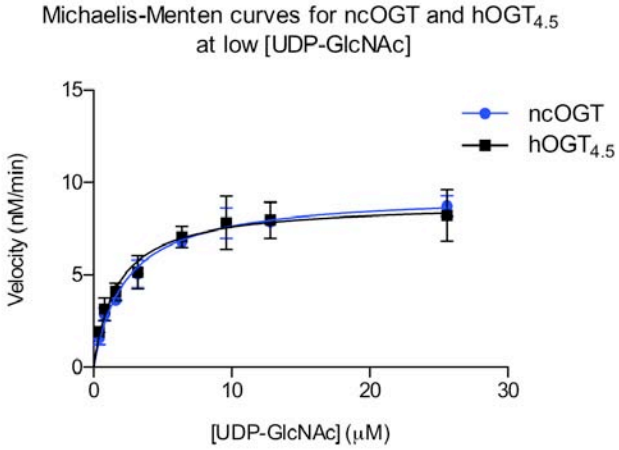

d

Kinetic constants	ncOGT	$hOGT_{4.5}$
K_m UDP-GlcNAc (μM)	2.3 ± 0.36	1.8 ± 0.47
k_{cat} (min^{-1})	0.29 ± 0.012	0.22 ± 0.015
k_{cat} / K_m (min^{-1} μM^{-1})	0.12 ± 0.014	0.13 ± 0.025

Supplementary Figure 1. Kinetics of ncOGT and $hOGT_{4.5}$ with the CKII3K peptide. Assays were performed using 3 mM CKII3K peptide[1,2] while varying the concentration of UDP-^{14}C-GlcNAc (diluted with cold UDP-GlcNAc as required). Reactions were run for 30 min at room temperature with 32 nM of ncOGT and 40 nM of $hOGT_{4.5}$ for the lower concentrations of UDP-GlcNAc (between 0.4 and 50 μM) and 600 nM enzyme for the higher Km measurements (for UDP-GlcNAc between 50 μM and 4 mM). Data were analyzed by GraphPad Prism5. **a and b,** Eadie-Hofstee plots of ncOGT and $hOGT_{4.5}$, respectively. Two distinct Kms for UDP-GlcNAc are observed. For greater accuracy, the Km values shown on the plots were determined by nonlinear regression analysis of the velocity versus substrate concentration curves (see **1c** for an example). **c,** ncOGT and hOGT4.5 at saturating (3mM) CKII3K peptide concentrations and UDP-GlcNAc concentrations below 30 μM, performed in duplicate. At UDP-GlcNAc levels below 30 μM, ncOGT and $hOGT_{4.5}$ display Michaelis-Menten behavior. Except for the data shown in Supplementary Figs. 1a and 1b, all kinetic experiments described in the manuscript were carried out at [UDP-GlcNAc] below 30 μM. (Graphpad Prism5; average ± s.e.m., n=2) **d,** Kinetic constants derived from the data shown in **c**. The lower Km value for UDP-GlcNAc is similar to previously reported values.[1,3] (Graphpad Prism5; average ± s.e.m., n=2, error calculated from nonlinear regression of entire curve in duplicate).

Supplementary Figure 2

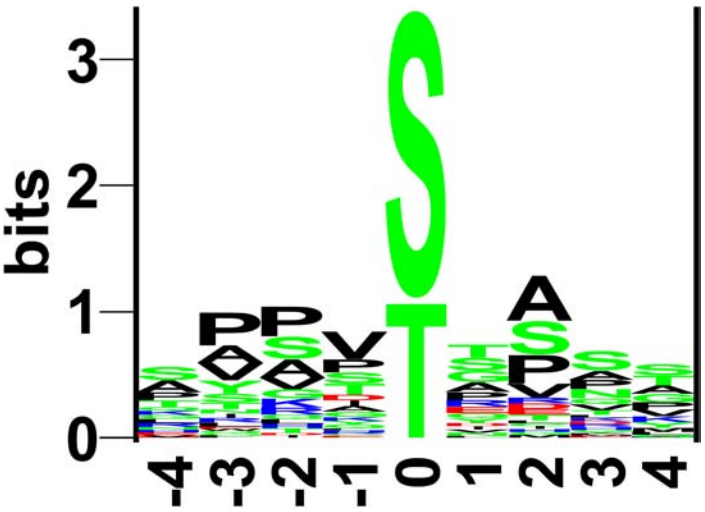

Supplementary Figure 2. A sequence logo generated from proteins where the exact site of O-GlcNAcylation is known. The peptide sequences are listed in Supplementary Table 4. The peptides were aligned such that the glycosylation site is in the middle at the 0 position, and the sequence was then truncated to include only 4 residues to the N terminus of the glycosylation site ("-4") through 4 residues to the C-terminus of the site ("4"). The logo was generated using the online program "Protein Sequence Logos using Relative Entropy" [5,6].

Supplementary Figure 3

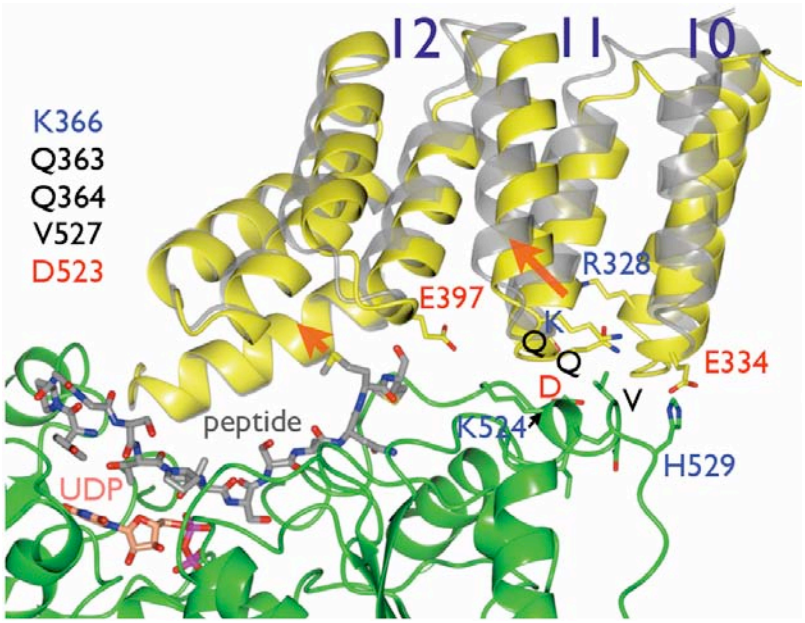

Supplementary Figure 3. Opening of the active site cleft. Superposition of the OGT-UDP structure (yellow) and the OGT-UDP-peptide structure (gray) shows the movement of the TPRs upon substrate binding. The peptide (shown as a gray stick model) juts into TPR 12 (left arrow), which hinges open the cleft. Opening of the cleft is due to a hinge-like movement between TPRs 12 and 13, which results in a 6 Å shift of TPR 10 away from the catalytic domain compared with the OGT-UDP structure. In the OGT-UDP structure, the first two TPR repeats of the $hOGT_{4.5}$ construct (corresponding to TPRs 10 and 11 of ncOGT) make several contacts with the sidechains of helix H2, such as H529 and E334, in order to keep the TPR domain latched to the catalytic region.

Supplementary Figure 4

a

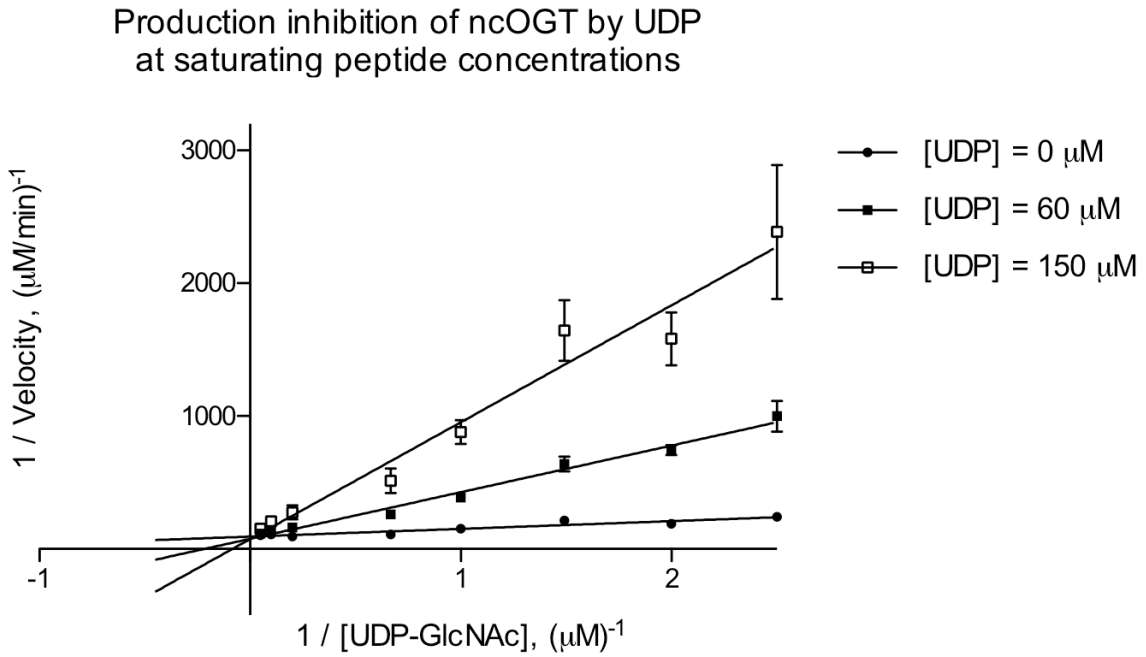

b

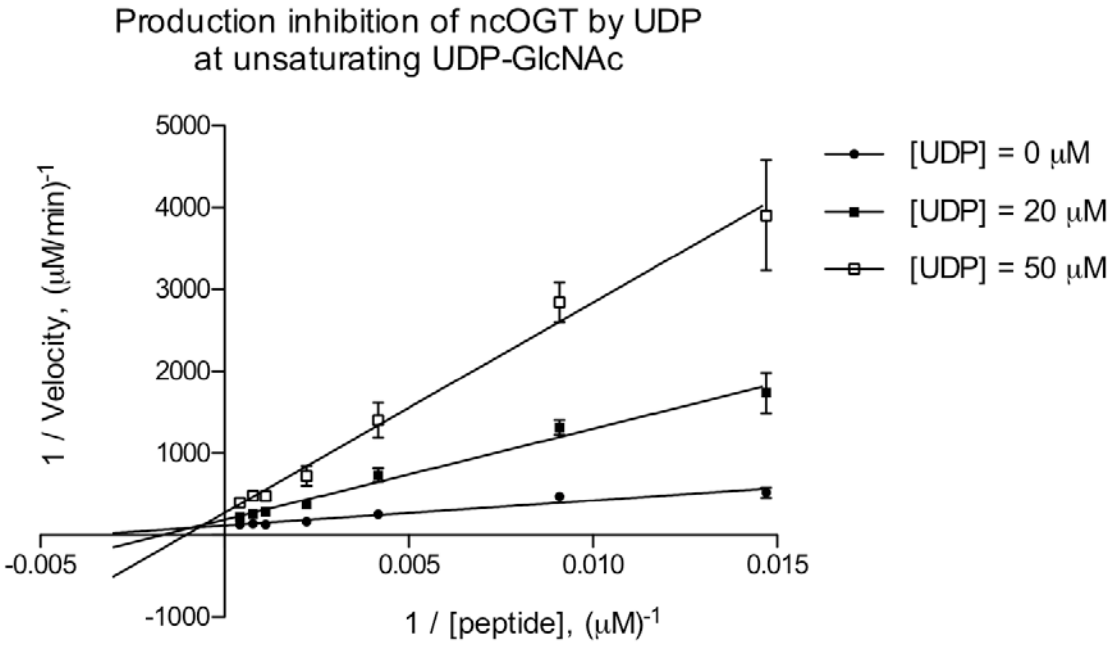

Supplementary Figure 4. Product inhibition patterns by UDP support an ordered bi bi mechanism. a, Double reciprocal plot showing inhibition of ncOGT by UDP at saturating peptide concentrations (Graphpad Prism5; average ± s.e.m., n=3)**.** Reactions were performed in the presence of UDP at saturating peptide concentrations while varying UDP-GlcNAc levels (conditions: 80 nM purified ncOGT, 3.5 mM CKII3K peptide, UDP-GlcNAc varied from 0.625 to 30 μM, and UDP at the indicated, fixed concentrations; 30 minute incubation at room temperature). For a random bi bi mechanism at saturating peptide concentrations, no inhibition by UDP should be observed; for an ordered mechanism with UDP-GlcNAc binding first and UDP leaving last, UDP should be a competitive inhibitor with respect to UDP-GlcNAc under these conditions[7,8]. Linear regression analysis of the data is consistent with competitive inhibition (Vmax of ~0.01 μM/min) **b,** Double reciprocal plot showing inhibition of ncOGT by UDP at unsaturating UDP-GlcNAc conditions (Graphpad Prism5; average ± s.e.m., n=3). Reactions were performed in the presence of UDP and unsaturating UDP-GlcNAc (1.2 μM) while varying peptide concentrations from 68 μM to 2.4 mM. Mixed inhibition, as observed, is expected for an ordered mechanism in which UDP-GlcNAc binds first, but it is not consistent with a rapid equilibrium random mechanism[7,8]. For 0, 20, and 50 μM UDP, Vmax values of 0.01, 0.006, and 0.003 μM/min were calculated, respectively.

Supplementary Figure 5

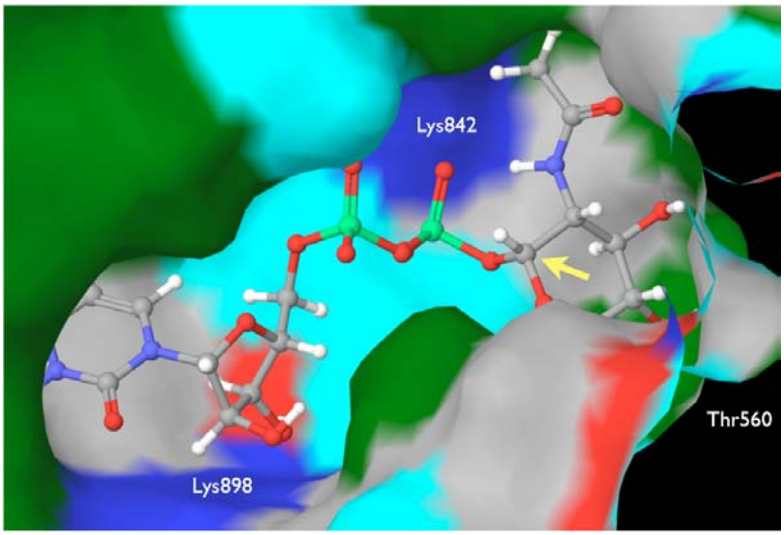

Supplementary Figure 5. Structure of UDP-GlcNAc docked into the active site. This fit is the highest ranking pose with a docking score of -12.785. The OGT-UDP structure was used to build energy grids using the default value of protein atom scaling (1.0) within a cubic box with sides of 24 Å. The ligand and protein were parametrized with the OPLS2001 force field. Docking calculations were performed in Extra Precision mode. Generated ligand poses were scored by GlideScore[9]. Residues visible in this cut away view that make critical contacts with UDP-GlcNAc are indicated. The sidechain of His901 (not shown in the cutaway) also stacks directly over the uracil and we have confirmed its importance in catalytic activity via mutagenesis (Supplementary Table 3). The anomeric carbon of the GlcNAc residue is indicated by the yellow arrow. In this conformation, the β face of the sugar is exposed to the peptide, consistent with the proposed mechanism involving a displacement of UDP with inversion of configuration. A lower ranking pose in which the N-acetyl group points down into the pocket is sterically feasible and is consistent with the conformation observed in a complex of a bacterial OGT homolog bound to a UDP-GlcNAc C-glycoside analog[10]. However, the lower ranking pose is not consistent with the enzymatic reaction or with experimental evidence that the N-acetyl group of the GlcNAc is solvent exposed[2].

Supplementary Figure 6

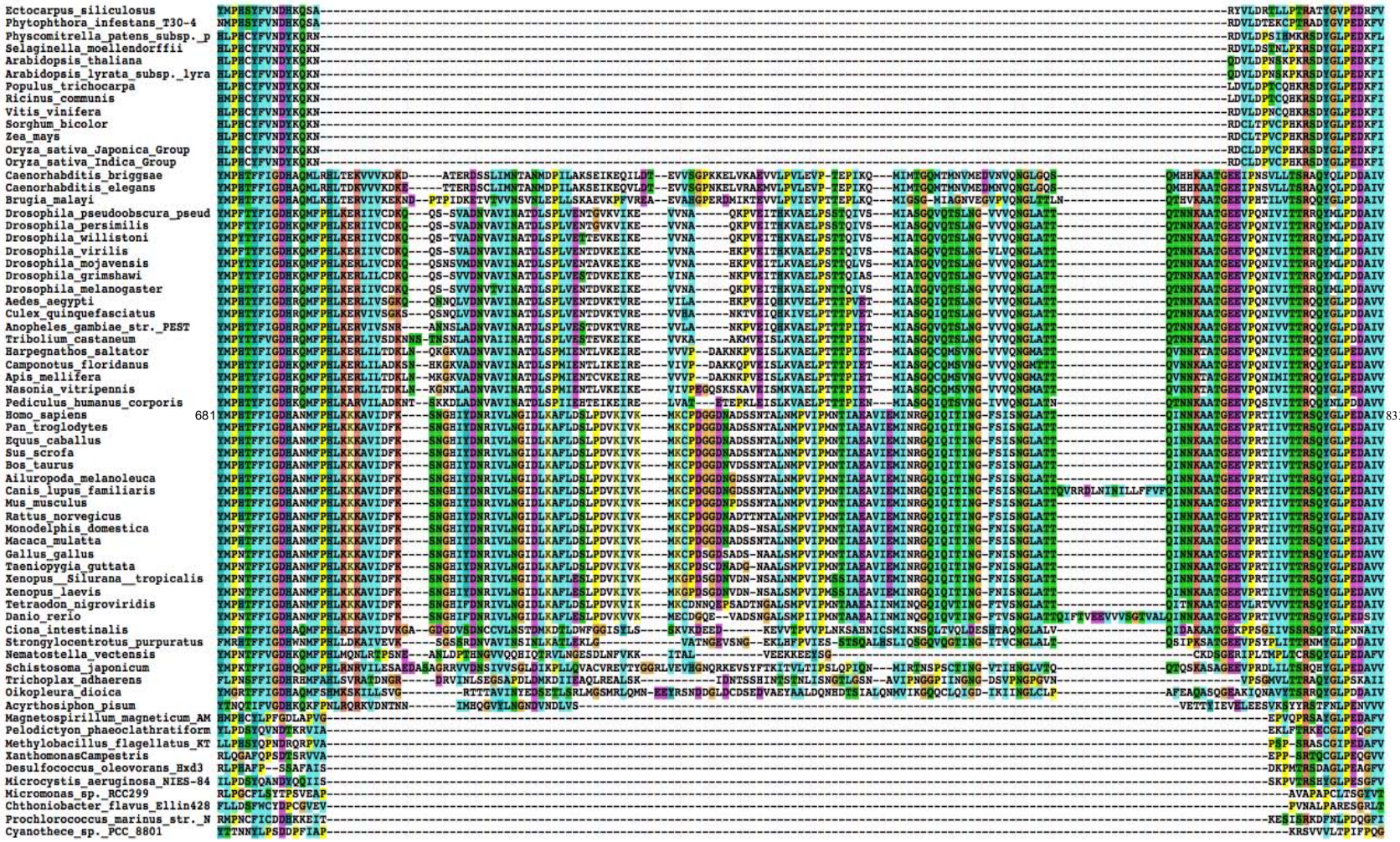

Supplementary Figure 6. Evolutionary Conservation of the Intervening Domain. Regions corresponding to or flanking the Int-D domain from a range of OGT homologs were aligned using CLUSTALX[4]. The blue bracket on the left indicates the proteins from metazoans; the red bracket indicates homologs that belong to chordates. The intervening domain is present only in metazoans. The lysines in the intervening domain are conserved among chordates and are highlighted with red boxes or dotted lines. The blue arrows indicate domain boundaries for the intervening domain. The boundaries numbers are indicated for human OGT.

Supplementary Figure 7

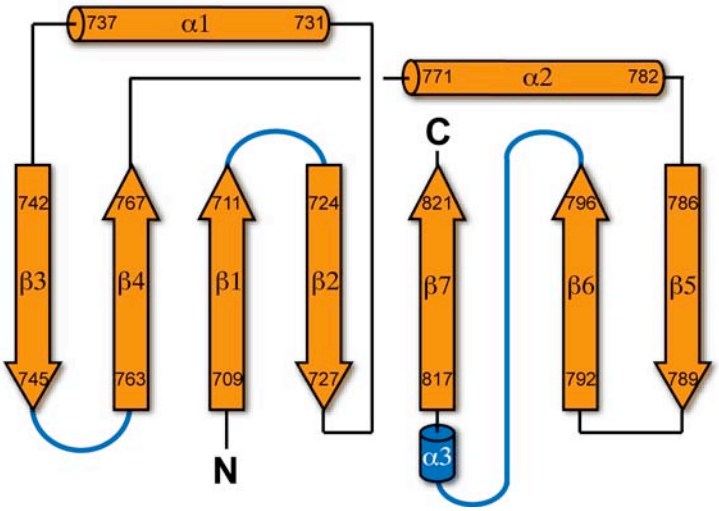

Supplementary Figure 7. Topology diagram of the intervening domain of OGT (spanning residues 698-827, approximately). α-helices are represented by cylinders and β-strands are represented by arrows. Residue boundaries of secondary structure elements are numbered. The three large loops of the domain are shown in blue. In the structures, electron density is missing for twelve residues in the β3-β4 loop and for four residues in the β1-β2 loop.

Supplementary Figure 8

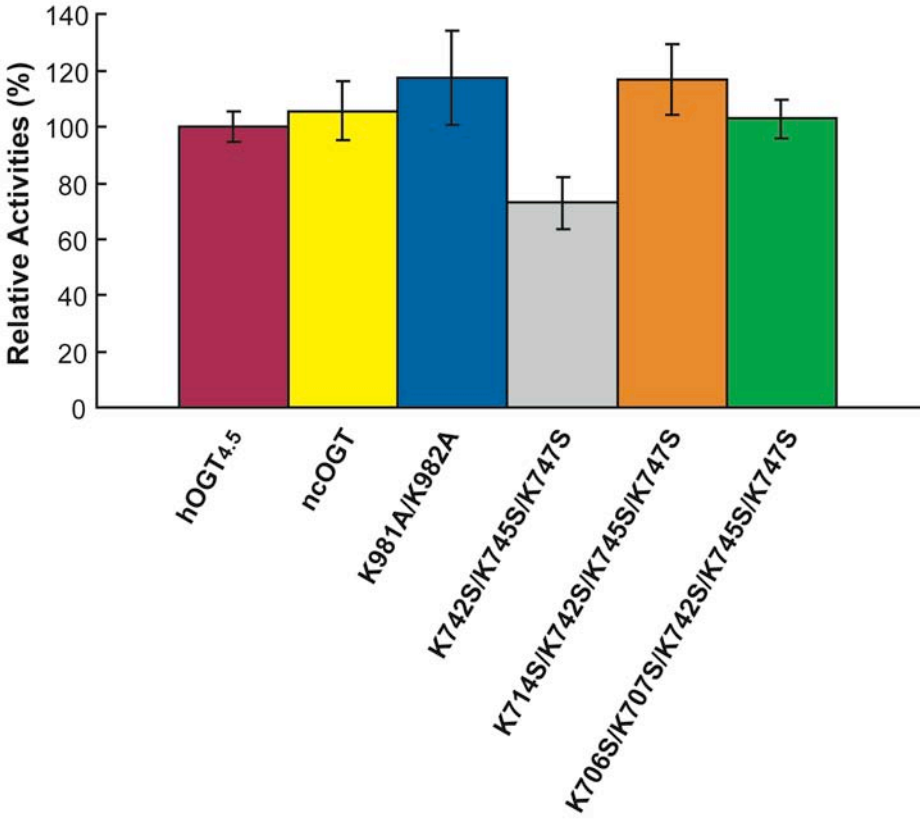

Supplementary Figure 8. Relative activities of OGT Int-D domain mutants that contribute to the positively charged patch depicted in Figure 3b. The activities of Int-D domain mutants listed in Supplementary Table 3 were measured using the previously reported CKII peptide filter-binding assay[2] (average ± s.d., n=3). The activity of the K981/K982 mutant is consistent with previous reports[11].

Supplementary Figure 9

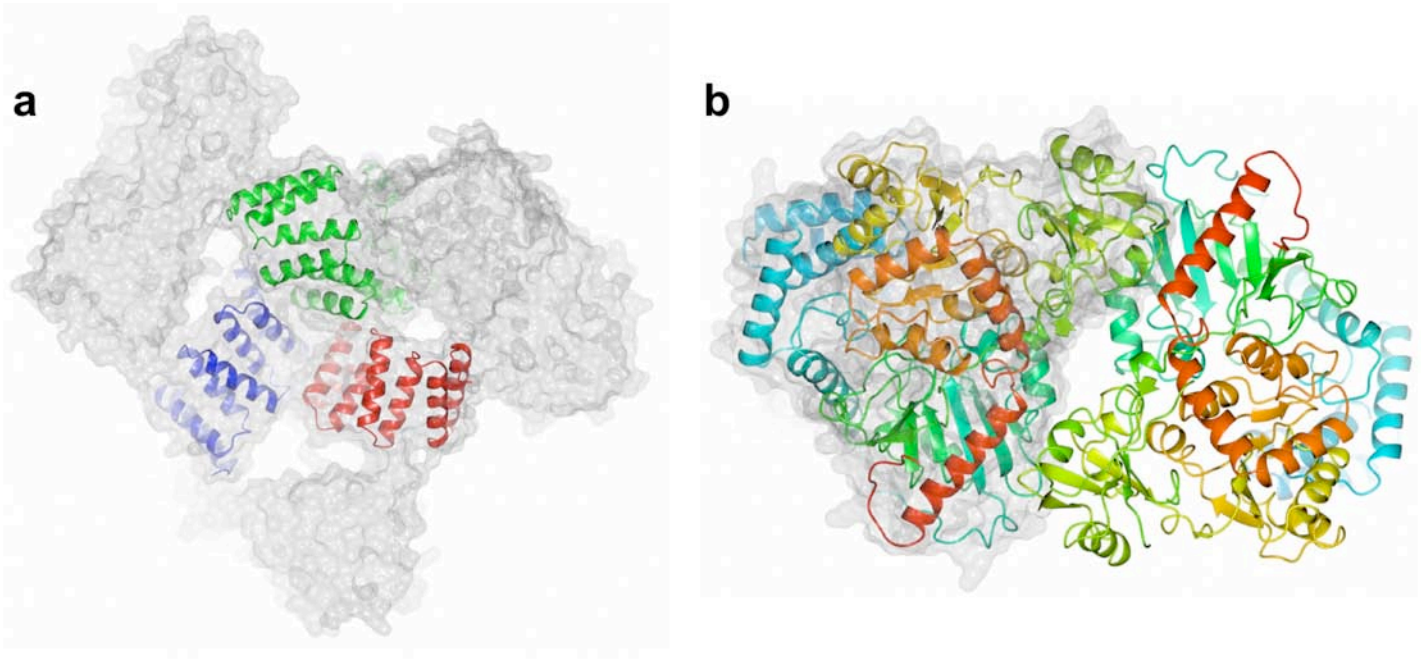

Supplementary Figure 9. Crystal Packing Interfaces. a, OGT-UDP crystal packing. OGT-UDP crystallized with four copies in the asymmetric unit in the P321 space group, but there is a threefold symmetry interface, as shown. This trimer is not relevant for the full-length protein since it would not be able to form if there were more than 4.5 TPR units. **b,** OGT-UDP-CKII crystal packing. The OGT-UDP-CKII complex crystallized in the I121 space group as a dimer, as shown. We do not interpret any of the several observed multimerization surfaces as physiologically relevant since equilibrium sedimentation ultracentrifugation experiments and gel filtration studies using the crystallization construct show that it is monomeric in solution.

Supplementary Tables

Supplementary Table 1. X-ray data collection and model refinement statistics of OGT-UDP and OGT-UDP-peptide complexes.

	UDP Complex	UDP-CKII Peptide Complex
Data Collection Statistics		
Beam Line	NSLS x29	NSLS x25
Space Group	P321	I121
Wavelength (Å)	1.0809	1.0000
Number of Reflections	154231	141571
Cell dimensions		
a, b, c (Å)	273.66, 273.66, 143.05	98.54, 136.66, 153.54
α, β, γ (°)	90.0, 90.0, 120.0	90.0, 102.90, 90.0
Resolution (Å)[a]	50-2.78 (2.93 - 2.78)	30-1.95 (2.06-1.95)
Rsymm[a]	0.116 (0.425)	0.098 (0.180)
I/σI[a]	8.4 (3.0)	8.4 (4.7)
Completeness (%)[a]	98.2 (95.1)	98.4 (94.5)
Redundancy[a]	3.3 (3.1)	3.1 (2.8)
Average mosaicity	0.47	0.43
Refinement Statistics		
Resolution (Å)	50 - 2.78	30-1.95
No. Reflections	151011	141555
Reflections (work/test)	148987 / 2024	134456 / 7099
Rwork / Rfree %	18.5 / 21.8	22.4 / 25.2
Number of OGT molecules/asymmetric unit	4	2
Number of modeled OGT residues/chain	701	695 for chain A / 674 chain C
Number of water molecules	286	860
Number of SO_4 ions		3
Average B-Factors		
OGT	50.0	21.7
UDP	37.8	9.4
Peptide		20.1
Solvent	37.0	24.1
R.m.s deviations		
Bond Lengths (Å)	0.003	0.007
Bond Angles (°)	0.707	1.050
Ramachandran (number of residues / %)		
Allowed	2778 / 99.9%	1416 / 100.0%
Favored	2706 / 97.3 %	1390 / 98.2 %
Disallowed	2 / 0.07 %	0 / 0 %
Residues in disallowed region	Pro B859, C859	

[a]Values in parentheses are from highest resolution shell.

Supplementary Table 2. X-ray data collection statistics of heavy atom derivatives.

	Potassium platinum tetrachloride derivative	Sodium aurothiomalate derivative	Potassium platinum tetrabromide derivative	Potassium platinum tetrachloride derivative
Data Collection Statistics				
Beam Line	BNL x29	APS ID24C	BNL x29	BNL x29
Space Group	P321	P321	P321	P321
Wavelength (Å)	1.0715	1.0384	1.0715	1.0715
Number of Reflections[a]	38280 (5632)	30134 (4412)	12120 (1768)	92019 (13411)
Cell dimensions				
a, b, c (Å)	273.2, 273.2, 142.8	274.3, 274.3, 143.0	271.9, 271.9, 141.9	274.1, 274.1, 142.7
α, β, γ (°)	90.0, 90.0, 120.0	90.0, 90.0, 120.0	90.0, 90.0, 120.0	90.0, 90.0, 120.0
Resolution (Å)[a]	45-4.4 (4.64-4.40)	42-4.8 (5.06-4.80)	48-6.5 (6.85-6.5)	49-3.3 (3.48-3.30)
Rsymm[a]	0.107 (0.409)	0.095 (0.382)	0.072 (0.358)	0.099 (0.346)
I/σI[a]	8.4 (3.5)	9.9 (4.2)	15.6 (4.3)	9.7 (4.0)
Completeness (%)[a]	98.1 (99.5)	98.8 (99.6)	99.5 (100.0)	99.5 (99.9)
Redundancy[a]	3.8 (3.8)	4.1 (4.2)	5.2 (5.3)	3.9 (3.9)
Overall isomorphous phasing power acentric	1.27	1.16	1.40	1.05
Overall isomorphous phasing power centric	1.11	1.10	1.02	0.74
Overall anomalous phasing power	0.78	0.61	1.42	0.541

[a]Values in parentheses are from highest resolution shell.

Supplementary Table 3. Summary of the enzymatic activity of OGT mutants reported in the literature and made in this study.

Mutant	<10% Activity	10-30% Activity	30-60% Activity	60-100% activity	Reference
D431A				×	(10)
N458A				×	(10)
H498A	×				this study and (10)
H499A			×		this study
D523A	×				(12)
H558A	×				this study and (13)
R637A	×				(10)
Q839N	×				(13)
Y841A				×	(13)
K842A	×				(13)
K842M	×				(13)
K898A	×				(10) and (13)
H901A	×				this study
H920A	×				(13)
T921A		×			(13)
D925A	×				(10)
K981A/K982A				×	this study and (11)
K742S/K745S/K747S				×	this study
K714S/K742S/K745S/K747S				×	this study
K706S/K707S/K742S/K745S/K747S				×	this study

Mutants made by us were tested as described in Methods.

Supplementary Table 4. O-GlcNAcylation sites on OGT protein substrates reported in the literature.

Peptide	Protein Source	GI No.	Ref. No.
EEKPAV**T**AAPK	Rat α-crystallin B chain	203613	(14)
AERAIPV**S**REEKPSSAPSS	Human α-A-crystallin	2827909	(1)
FELLP**T**PPLSPSR	Human c-Myc	158516267	(14)
SHYGG**S**LPNVNQIGC	Human CRTC2/TORC2	32171215	(14)
LNRTS**S**D**S**ALHTSVMNPNP	Human CRTC2/TORC2	32171215	(14)
TVSTMPHT**S**GMNRLTQ	Human FoxO1	9257222	(14)
QSFPHSVKT**T**THSWV**S**G	Human FoxO1	9257222	(14)
STFRPR**T**SSNASTISGRLSP	Human FoxO1	9257222	(15)
APPPS**S**TASASASV	Rat IRS-1	6981106	(14)
SPGEYVNIEFGSGQPGYLAGPAT**S**RSSPSVRC	Rat IRS-1	6981106	(16)
QSYVDTSPVAPV**S**YADMR	Rat IRS-1	6981106	(16)
KVSLPRTTGAAPPPSATASA**S**ASVTPQGAAE	Rat IRS-1 (S1036A)	6981106	(16)
QSYVDTSPAAPV**S**YADMR	Human IRS-1	5031805	(16)
INPSVNPGI**S**PAHGVTR	Rat NCOA1/SRC-1	157819661	(14)
SSRQVAH**S**GAKTSVV	Rat OGA	16943639	(14)
CPVQLWVD**S**TPPPGTR	Human p53	23491729	(14)
HDTSASTQSTPAS**S**RAQTLPT	Rat Spectrin β2	34879632	(14)
KSPVV**S**GDTSPR	Rat microtubule associated protein	517394	(17)
EQVTNVGGAVV**T**GVTAVAQK	Rat α-Synuclein	122066261	(17)
TKEQANAV**S**EAVVSSVNTVATK	Rat γ-Synuclein	122066261	(17)
AAAEKTKQGV**T**EAAEKTK	Rat β-Synuclein	77404215	(17)
TPTVVRI**T**VAPGALER	Rat host cell factor C1	213385315	(17)
EPAK**T**QPMVAAAA**TT**TTTTTTTVAEK	Rat methyl-CpGbinding protein 2	149029883	(17)
SMPGGSTPV**S**SANMMSGIS	Human CKII	29570793	(1)
SPNSPSY**S**P**T**SPSYSPS**S**PSYSPT	Drosophila RNA polymerase II CTD	7292659	(1)
SYSP**T**SPNYT	Calf thymus RNA polymerase II	119911821	(18)
KYSP**T**SP**T**YSPTS	Calf thymus RNA polymerase II	119911821	(18)
LLTAQTIT**S**ETPSSTTTTQITKTVKGGISE	Human Band 4.1	55664328	(1)
KQAAFGG**S**GPRATDKDT	Mouse RecQ protein-like 4	110815828	(19)
SPGRAPKG**S**RRSVAASHEGD	Mouse Lamin B receptor	148681171	(20)
FFSSLSNAVKQ**T**TAAAAATFSEQVGGGSGGA	Rat Syn I	9507159	(20)
GATPGSAAASAERA**S**TAAPVASPAAPSPGSSG	Rat Syn I	9507159	(20)
LPSPTAAPQQ**S**ASQATPMTQGQGR	Rat Syn I	9507159	(20)
RPVDQLRHLLV**S**NVGGDGEEIERFFKL	Rat Nucleoporin 155	149016472	(20)
LNMAGGPADT**S**DPLQQICKI	Rat Nuclear Pore Protein p62	71894951	(21)
RARY**S**ECSGTQGSHSTK	Rat PGC-1a	13786188	(22)
KFSSPIVK**S**TEANVLPPS**S**IGFTFSVPVAK	Human NUP153	31418202	(23)
TITVPV**S**GSPKMSN	Human EMSY	9923559	(23)
YSTRSAPA**S**QASLRATS	Human NUMA	71361682	(23)
TVPSSTSKD**S**PVSQPSLVGSK	Human erythrocyte 65-kD protein	41688795	(18)
NYLAPV**S**ASVSP**S**AV**S**SANGTV	Human serum response factor	4507205	(18)
KRRYVE**T**PRVHI**S**SVRSGY	Rat neurofilament (NF-L)	226783	(18)
WSRGSPS**T**VSSSYK	Rat neurofilament (NF-M)	56752	(18)
THRQPSV**T**ISSKIQK	Rat neurofilament (NF-M)	56752	(18)
PPSVPV**S**GSAPGRLS	HHV-5 HCMV (UL32) BPP	270356127	(18)
STTPTYPAVTTVYPPS**S**TAKSSVSN	HHV-5 HCMV (UL32) BPP	270356127	(18)
VTNLPGTT**S**TIQTAPSTSTT	Human serum response factor	4507205	(18)
QMACQNLVDPAC**T**QSQVLSAATIVAKH	Chicken talin	26000436	(18)
GILANQL**T**NDYGQLAQQ	Chicken talin	26000436	(18)

Only sequences containing known GlcNAcylation sites have been listed. The glycosylation sites are shown in bold red.

Supplementary Table 5. PIP binding mutants.

Construct (in GST-ncOGT background)	Mutations introduced
WT	Wildtype
Mut1	K981A/K982A
Mut2	K706S/K707S/K742S/K745S/K747S
Mut3	K714S/K742S/K745S/K747S
Mut4	K981E/K982E/K986E/K989E
Mut5	K742E/K745E/K747E

The listed point mutations were introduced into full-length ncOGT fused to N-terminal glutathione-S-transferase (GST). The wildtype and mutant constructs were tested for binding to commercially available PIP arrays as described in Methods. Wildtype GST-ncOGT binds to PtdIns(3,4,5)P_3, as previously described[11], although we observed that it also binds to PtdIns(3,4)P2, PtdIns(3,5)P2, PtdIns(4,5)P2, and phosphatidic acid. The mutants, including the previously reported K981A/K982A mutant, showed similar binding behavior as GST-ncOGT in PIP binding assays under the assay conditions (see Methods). Removal of the GST domain abrogated binding of the wildtype ncOGT to the PIP arrays, indicating that binding is GST-dependent. Since full experimental details were not described in the previously reported studies, we cannot compare our results to those directly.

Supplementary Table 6. Primers used to make OGT mutants in this study.

Primer	Sequence (5' to 3')
H498A forward	CACCCGGCTCACTCTATGCTGTACCCGCTGTCTCACGG
H498A reverse	TAGAGTGAGCCGGGTGAACAGACGGCAGACGGTTTTTTTCC
H499A forward	GCACGCTTCTATGCTGTACCCGCTGTCTCACGG
H499A reverse	TAGAAGCGTGCGGGTGAACAGACGGCAGACGG
H558A forward	TAACGCTCCGACCTCTCACCTGATGCAGTCTATCC
H558A reverse	TCGGAGCGTTACCGAAGTCAGAAGAAACGTAACC
H901A forward	AGAAGCTGTTCGTCGTGGTCAGCTGGCTGACGTTTGC
H901A reverse	ACGAACAGCTTCTTCTTTCGGAGCAACCGGAGAGAAGATG
K981A/K982A forward	CCTGGCTGCTGTTCGTGGTAAAGTTTGGAAACAGC
K981A/K982A reverse	GAACAGCAGCCAGGTATTCCAGGTCGGTACCCAG
K742S/K457S/K747S forward	CGTTTCTATCGTTTCTATGTCTTGCCCGGACGGCGGTGACAACGCTG
K742S/K457S/K747S reverse	GGCAAGACATAGAAACGATAGAAACGTCCGGCAGAGAGTCCA GGAAAGC
K706S/K707S forward	CACCTGTCTTCTAAAGCTGTTATCGACTTCAAATCTAACGG
K706S/K707S reverse	CTTTAGAAGACAGGTGCGGGAACATGTTAGCGTGGTC
K714S forward	GACTTCTCTTCTAACGGTCACATCTACGACAACCGTATC
K714S reverse	GTTAGAAGAGAAGTCGATAACAGCTTTTTTTTTCAGGTGC
4.5TPR_HRV_site forward	TCCGCTGGAAGTTTTGTTCCAAGGTCCGGGTTCTTGCCCGACCCACGCTGACTCTCTG
4.5TPR_HRV_site reverse	GGCAAGAACCCGGACCTTGGAACAAAACTTCCAGCGGATCCCGACCCATTTGCTGTCC
8His forward	TCCGCACCATCACCATCACCATCACCACCTGGAAGTTTTGTTCCAAGGTCCG
8His reverse	CCAGGTGGTGATGGTGATGGTGATGGTGCGGATCCCGACCCATTTGCTGTCCAC
C term_no_His forward	TGAATAACACCACCACCACCACCACCACCACTAATTG
C term_no_His reverse	GGTGGTGTTATTCAACCGGTTTAATCATGTGGTCCGG

Supplementary Movie 1. Molecular dynamics simulations of OGT. This movie is based on a 1 microsecond simulation and shows the global movement of the TPRs based on motion of the hinge described in Supplementary Figure 3.

Coordinate Models. The following models are available for download from the Walker lab web site (http://www.chem.harvard.edu/groups/walker/ogt.htm).

Model 1. PDB coordinates for the model of ncOGT bound to UDP. As described in the caption of Fig. 3c, this full-length model was prepared by combining our OGT-UDP structure (PDB code 3PE3) with the OGT TPR structure (PDB code 1W3B).

Model 2. PDB coordinates for the model of ncOGT bound to UDP and the CKII peptide. Model of the full length OGT-UDP-peptide structure assembled from our complex structure (PDB code 3PE4) and the OGT TPR structure (PDB code 1W3B).

Model 3. PDB coordinates for the model of UDP-GlcNAc docked into hOGT4.5. UDP-GlcNAc was docked into the OGT-UDP structure (see Supplementary Fig. 5).

References

1. Kreppel, L.K. & Hart, G.W. Regulation of a cytosolic and nuclear O-GlcNAc transferase. Role of the tetratricopeptide repeats. *J Biol Chem* **274**, 32015-22 (1999).
2. Gross, B.J., Kraybill, B.C. & Walker, S. Discovery of O-GlcNAc transferase inhibitors. *J Am Chem Soc* **127**, 14588-9 (2005).
3. Lubas, W.A. & Hanover, J.A. Functional expression of O-linked GlcNAc transferase. Domain structure and substrate specificity. *J Biol Chem* **275**, 10983-8 (2000).
4. Larkin, M.A. et al. Clustal W and Clustal X version 2.0. *Bioinformatics* **23**, 2947-8 (2007).
5. Gorodkin, J., Heyer, L.J., Brunak, S. & Stormo, G.D. Displaying the information contents of structural RNA alignments: the structure logos. *Comput Appl Biosci* **13**, 583-6 (1997).
6. Schneider, T.D. & Stephens, R.M. Sequence logos: a new way to display consensus sequences. *Nucleic Acids Res* **18**, 6097-100 (1990).
7. Segel, I.H. *Enzyme kinetics : behavior and analysis of rapid equilibrium and steady state enzyme systems*, xxii, 957 p. (Wiley, New York, 1975).
8. Copeland, R.A. *Enzymes : a practical introduction to structure, mechanism, and data analysis*, xvi, 397 p. (Wiley, New York, 2000).
9. Schrödinger Software Suite. (Schrodinger LLC, New York, 2006).
10. Clarke, A.J. et al. Structural insights into mechanism and specificity of O-GlcNAc transferase. *Embo J* **27**, 2780-8 (2008).
11. Yang, X. et al. Phosphoinositide signalling links O-GlcNAc transferase to insulin resistance. *Nature* **451**, 964-9 (2008).
12. Lazarus, B.D., Roos, M.D. & Hanover, J.A. Mutational analysis of the catalytic domain of O-linked N-acetylglucosaminyl transferase. *J Biol Chem* **280**, 35537-44 (2005).
13. Martinez-Fleites, C. et al. Structure of an O-GlcNAc transferase homolog provides insight into intracellular glycosylation. *Nat Struct Mol Biol* **15**, 764-5 (2008).
14. Copeland, R.J., Bullen, J.W. & Hart, G.W. Cross-talk between GlcNAcylation and phosphorylation: roles in insulin resistance and glucose toxicity. *Am J Physiol Endocrinol Metab* **295**, E17-28 (2008).
15. Housley, M.P. et al. O-GlcNAc regulates FoxO activation in response to glucose. *J Biol Chem* **283**, 16283-92 (2008).
16. Klein, A.L., Berkaw, M.N., Buse, M.G. & Ball, L.E. O-linked N-acetylglucosamine modification of insulin receptor substrate-1 occurs in close proximity to multiple SH2 domain binding motifs. *Mol Cell Proteomics* **8**, 2733-45 (2009).
17. Wang, Z. et al. Enrichment and site mapping of O-linked N-acetylglucosamine by a combination of chemical/enzymatic tagging, photochemical cleavage, and electron transfer dissociation mass spectrometry. *Mol Cell Proteomics* **9**, 153-60 (2010).
18. Hart, G.W. & Akimoto, Y. The O-GlcNAc modification. *Essentials of glycobiology*, chapter 18.
19. Khidekel, N. et al. Probing the dynamics of O-GlcNAc glycosylation in the brain using quantitative proteomics. *Nat Chem Biol* **3**, 339-48 (2007).
20. Wells, L. et al. Mapping sites of O-GlcNAc modification using affinity tags for serine and threonine post-translational modifications. *Mol Cell Proteomics* **1**, 791-804 (2002).
21. Lubas, W.A., Smith, M., Starr, C.M. & Hanover, J.A. Analysis of nuclear pore protein p62 glycosylation. *Biochemistry* **34**, 1686-94 (1995).
22. Housley, M.P. et al. A PGC-1alpha-O-GlcNAc transferase complex regulates FoxO transcription factor activity in response to glucose. *J Biol Chem* **284**, 5148-57 (2009).
23. Wang, Z. et al. Extensive crosstalk between O-GlcNAcylation and phosphorylation regulates cytokinesis. *Sci Signal* **3**, ra2 (2010).